Simulations of Primary Beam Truncation and Pointing Errors with the MMA

ROBERT BRAUN

National Radio Astronomy Observatory,[a] Socorro, New Mexico 87801

INTRODUCTION

This memo is one in a series investigating the applications and limitations of mosaicing, the imaging of objects large with respect to an interferometer primary beam using multiple pointings, with a particular emphasis on identifying design constraints for the proposed MMA. In this case we consider the results of a series of simulations of noiseless mosaic observations and their subsequent reconstruction. First we consider the quality of reconstruction possible with only limited knowledge of the primary beam pattern used in the simulated observation. Secondly we explore the quality of reconstruction possible when the simulated observations suffer from pointing errors.

BASIC MOSAIC SIMULATION

The basic ingredients of a simulation experiment are a description of the interferometric array, a model brightness distribution and an observing run specification. Subsequently, the simulated data must be reduced in a comparable fashion to data that was actually observed.

In order to investigate the performance of a MMA in application to very extended sources it was appropriate to consider a rather compact configuration. The current strawman concept calls for $\sim$ 40 antennas of $\sim$ 7.5 m diameter commonly operating at 230 GHz. Recent configuration studies (Cornwell, 1988; Hjellming, 1988) have shown how (pseudo-) randomly filled circular configurations give rise to a uniform (2-D) density of sampled baselines out to the maximum baseline observed. In the continuous limit this corresponds to the recognition that the auto-correlation of a circle is a disk. The natural synthesized beam of such a configuration is the well known Jinc function with $\sim$ 10 % near-in sidelobes. Given the freedom to design a natural synthesized beam, it seems desirable to strive for a functional form which allows easy image interpretation with a minimum of further processing. While various functions might be considered for this role, an obvious choice is a Gaussian with its well known convolution relations. This function also allows trivial inversion of the continuous limit auto-correlation relation, i.e. a Gaussian distribution of antennas gives rise to a Gaussian distribution of baselines, with a Gaussian synthesized beam. With a finite number of elements it becomes necessary to take precautions to avoid the grating responses which arise from redundant spacings, either through local randomizing of antenna locations or close attention to the 2-D geometry. A reasonably successful configuration based on this philosophy was designed consisting of three concentric rings at 12, 22 and 34 m radius on which 7, 17 and 15 telescopes were placed at regular intervals as shown

[a] The National Radio Astronomy Observatory (NRAO) is operated by Associated Universities, Inc., under the National Science Foundation Cooperative Agreement No. AST-8814515.

in Figure 1 and listed in Table 1. The largest deviation of the instantaneous natural synthesized beams with a Gaussian fit was in the 2 % near-in sidelobes as shown in Figure 2. The rather tight packing of this configuration results in a 40 % filling factor towards the zenith, while maintaining < 5 % shadowing losses within 30 degrees of the zenith. Global and/or north-south scaling could easily be implemented to extend hour-angle and/or declination coverage with minimal shadowing losses.

A model brightness distribution was obtained from an narrow band H_α CCD image of the large HII region complex in M31, Pellet 550, (Walterbos and Braun, 1989) by masking out background structure and subtracting off a base level. This model, illustrated in Figure 3, was chosen for its interesting mix of compact and extended structures and moderate degree of intrinsic dynamic range of about 300 to 1 (brightest to faintest structures present). Relative to the flat background the model dynamic range is of course much higher (about 10^6:1).

A simulated mosaic observation was carried out on the model shown in Figure 3 consisting of an 11 by 11 matrix of pointings separated by the antenna's HWHM of 22" at 230 GHz, with two 1 minute integrations per pointing spread between about -2 and $+2$ hours of hour angle. Noiseless cross-correlations were formed for all non-shadowed baselines as were the auto-correlations which were given a weight of 0.4 to match the geometrical filling factor of the configuration. Together, these resulted in the synthesized beam per pointing shown in Figure 2 with 3."5 FWHM. The 121 pointings were simultaneously deconvolved using the Maximum Entropy Method (MEM), which converged within 25 iterations to a stable solution. Both the total flux and source structure were accurately recovered in the post-convolved result at 3."5 resolution with a (peak/rms difference) dynamic range of 3000:1. The only notable shortcoming of the reconstruction was in a poorly defined base level in the outer 1/4 beamwidth of the mosaic pointing pattern. This underlines the need for restricting analysis of mosaic reconstructions to only properly sampled regions. The difference was formed between the smoothed model and the MEM result for the fully sampled central portion of the model image. The amplitude of the Fourier transform was averaged in annuli and normalized with the amplitude spectrum of the smoothed model. The normalized amplitude spectrum of residuals that results is shown in Figure 4. Inside of about 5 dish diameters (D) there is little structure in this spectrum. A minor peak of 0.4 % amplitude is seen at about 0.7 D, beyond which there is a gradual rise from 3 to 5 D and a major peak between 8 and 9 D at 7 % amplitude corresponding to the limit of the measured spacings. Most of the fractional discrepancies are arising at the highest spatial frequencies. It will be seen that the introduction of various sources of error will not significantly alter the shape of the residual spectrum but only result in an overall scaling.

Primary Beam Knowledge Truncation

The primary beam pattern which has been used to sample (and reconstruct) the model brightness distribution is the diffraction limited response of a uniformly illuminated 7.5 m aperture with a 0.75 m central circular blockage. This is meant to simulate the typical blockage due to a secondary mirror of a (sub-)mm telescope. Azimuthal assymetries which might arise, for example, from support legs have not yet

been introduced. The resulting pattern, illustrated in Figure 5, has its first null near 1 FWHM, and a broad 2 % amplitude sidelobe centered near 1.3 FWHM. Since in practice the knowledge of the primary beam response will inevitably be limited, it is important to consider the effects of incomplete or inaccurate data for the primary beam characteristics.

In order to explore the dependance of imaging fidelity on completeness of information on the primary beam, a series of simulations was carried out. The spatial scale of the model of Figure 3 was halved so that a 5 by 5 pointing mosaic would allow complete sampling. The simulated data (four, one minute integrations per pointing between H.A. = −0.83 and +0.83) was then reconstructed with a series of truncated primary beam models, which were identical to the sampling beam out to a given radius, but beyond which they were arbitrarily set to zero. The range of truncation radii considered was 0.5 to 1.3 FWHM. These reconstructions were then compared with the "standard" 1.6 FWHM reconstruction. The results of this comparison are shown in Figure 6a, in which the image peak to rms residual dynamic range is plotted as a function of truncation radius. The dynamic range of the reconstruction initially rises steadily with the beam truncation radius, levels out in a plateau near 1 FWHM and then rises again. This behaviour simply reflects the increasing contribution of the main lobe, the first null and inclusion of the first sidelobe in the reconstruction. The largest benefit is gained by knowledge of the main lobe down to the 3—5 % level at radii of 0.85 FWHM. Further gains come more slowly, and will in practise be more difficult to achieve. The fractional amplitude spectrum of residuals (as defined in the previous section) is shown in Figure 7 for the case of a truncation radius at 0.7 FWHM corresponding to a level of about 12 % on the main lobe. This spectrum is virtually featureless inside of 5 D, with an amplitude of a few %, after which it rises to almost 40 % at the longest observed baseline of about 9 D. Spectra for other truncation radii are almost identical, apart from a simple scaling with the dynamic range plotted in Figure 6a.

Since it may often be the case that only portions of much more extended objects will be imaged, it is interesting to consider the effect on imaging fidelity of this circumstance. The model above was "observed" with only a 3 by 3 pointing mosaic which severely undersamples the region of emission. Reconstructions were then made for the same range of beam truncation radii as above. The results shown in Figure 6b show the same trend seen for the fully sampled mosaics above although at only about one half the previous dynamic range. Fully sampling the region of emission is clearly desirable but not absolutely necessary.

Pointing Errors

Another potential source of image degradation comes from pointing errors. The severity of this effect was simulated with two simple approaches. In the first, the fully sampled 5 by 5 pointing mosaic above was given a fixed one dimensional offset for all the array telescopes with respect to the expected pointing position. Reconstructions were made for fixed offsets in the range 0.02 to 0.09 FWHM (corresponding to 1 to 4 arcsec with the above parameters). The dynamic range of these reconstructions relative the unshifted case is plotted in Figure 8a. Fixed offsets of even 0.02 FWHM already give significant degradation.

In the second approach, each pointing of the mosaic is given a random pointing offset in each of two dimensions with variances in the range 0.02 to 0.09 FWHM. Once again, all array telescopes participate in the same pointing offset, although the direction and amplitude now vary from one pointing to the next. The dynamic range achieved in these reconstructions is plotted in Figure 8b as a function of the pointing offset variance in units of the FWHM. As expected, the degradation in this case is significantly more severe than in the fixed 1-D case above, although the seemingly exponential functional form is similar. The fractional amplitude residual spectrum for the case of 0.02 FWHM variance is shown in Figure 9. This is similar to both Figures 7 and 4, although with larger amplitude and a somewhat earlier onset (at about 4 D) of high spatial frequency degradation.

Neither of these approaches is necessarily realistic, since in both cases all antennas are assumed to mispoint in the same sense, while in practice the antennas may be more likely to have uncorrelated pointing errors. On the other hand, long time scale (minutes) wind or differential heating induced mispointing may have a similar form. It is difficult to predict (and more challenging to simulate) how the reconstruction of uncorrelated pointing errors would differ from the case studied here since there are at least two competing effects. Consistency among the mosaic pointings is likely to improve by a factor $\sim \sqrt{n}$ for n antennas, while a systematic decorrelation introduced by the random antenna offsets will lead to a degradation in image fidelity for each individual pointing.

Summary

A number of conclusions can be drawn from the current series of studies. Interferometric array configurations with many elements can be tailored to give a desirable "natural" beam that requires only a minimum of deconvolution and allows straightforward image interpretation.

Mosaic observations and reconstructions of large fields requiring 100's of pointings on complex objects are feasible with only a single size element over the range of conditions considered here and very likely in actual circumstances. Reconstruction fidelity, as measured by the fractional amplitude residual spectrum, is good over a wide range of spatial frequencies. Specifically, the crucial transition region from auto- to cross-correlations at D/2 shows little structure over a wide range of error conditions as seen in Figures 4, 7 and 9. Incomplete knowledge of the antennas' primary beam pattern and pointing errors primarily give rise to a global scaling to higher amplitude of the residual spectrum with some redistribution of relative errors between high and intermediate spatial frequencies. The introduction of these error conditions generally leads to a more nearly uniform residual spectrum.

Dynamic ranges of 1000:1 should be possible in reconstructions for which the primary beam is known to only the few % level of the main lobe (cf. Figure 6a) although poorly sampled regions of more extended sources will likely suffer more than a factor 2 further degradation (cf. Figure 6b). This suggests that on-axis antenna designs will be quite adequate in allowing high fidelity imaging, since the sensitivity to far sidelobes is relatively small.

Pointing errors of the type and magnitude considered here present a serious limitation to image reconstruction. Correlated pointing errors, such as might arise from minute time-scale wind loading or differential heating, with a variance of only 0.02 FWHM (1 arcsec at 230 GHz with 7.5 m antennas) limit the dynamic range to about 300:1. Such errors should be kept at least a factor of two smaller in order not to unduly limit performance.

More extensive simulations are clearly needed and are already planned to explore various other effects; including realistic atmospheric degradation and uncorrelated pointing errors. However, the current study has already begun to address some of the important issues in the MMA design, underlining the utility of such an approach.

References

Cornwell, T.J. (1988), *IEEE Trans.Ant.Prop. 36, 1165.*

Hjellming, R. (1988), *in MMA design study, Vol. 2, NRAO.*.

Walterbos, R.A.M. and Braun, R. (1989), *Ap.J.Suppl., in prep.*

Figure Captions

Figure 1. A possible compact configuration for the MMA. Three concentric circles as 12, 22 and 34 m radius on which 7, 17 and 15 telescopes are placed at regular intervals to approximate a non-redundant Gaussian density distribution of the elements.

Figure 2. A cross-section of the synthesized beam obtained in two minutes integration with the configuration of Figure 1 operating at 230 GHz with a best-fit Gaussian overlaid.

Figure 3. A model brightness distribution used to test the imaging fidelity of the various simulations described in this document.

Figure 4. The normalized amplitude residual spectrum of an 11 by 11 pointing noiseless mosaic reconstruction of the model shown in Figure 3. The radial coordinate is in units of 0.277 D, so that the markings at 10, 20, 30 and 40 pixels correspond to 2.8, 5.6, 8.3 and 11.1 D.

Figure 5. A cross-section of the primary beam of a uniformly illuminated 7.5 m aperture with a central 0.75 m circular blockage.

Figure 6. a. Dynamic range (peak/rms residual) of a **fully sampled** (5 by 5 pointings on a spatially compressed version of Figure 3) mosaic reconstruction as a function of the imposed truncation radius of the primary beam model. **a.** Dynamic range (peak/rms residual) of a **poorly sampled** (3 by 3 pointings on a spatially compressed version of Figure 3) mosaic reconstruction as a function of the imposed truncation radius of the primary beam model.

Figure 7. The normalized amplitude residual spectrum of a fully sampled 5 by 5 pointing mosaic reconstruction for which the primary beam model was truncated at 0.7 FWHM. The radial coordinate is in units of 0.555 D, so that the markings at 5, 10, 15 and 20 pixels correspond to 2.8, 5.6, 8.3 and 11.1 D.

Figure 8. a. Dynamic range (peak/rms residual) of a fully sampled 5 by 5 pointing mosaic reconstruction as a function of the fixed one dimensional pointing offset introduced. **b.** Dynamic range (peak/rms residual) of a fully sampled 5 by 5 pointing mosaic reconstruction as a function of the variance of a random pointing offset in two dimensions between successive pointings in the mosaic.

Figure 9. The normalized amplitude residual spectrum of a fully sampled 5 by 5 pointing mosaic reconstruction for which random offsets in two dimensions with a variance of 0.02 FWHM were introduced. The radial coordinate is in units of 0.555 D, so that the markings at 5, 10, 15 and 20 pixels correspond to 2.8, 5.6, 8.3 and 11.1 D.

Table 1
Configuration Coordinates

X (m)	Y (m)	Z (m)
-6.81	-1.79	9.72
-3.44	-10.39	4.91
2.51	-11.17	-3.59
6.58	-3.54	-9.39
5.69	6.76	-8.12
0.51	11.97	-0.74
-5.05	8.16	7.21
-12.59	-1.35	17.99
-11.46	-9.20	16.37
-8.78	-15.79	12.55
-4.92	-20.26	7.02
-0.39	-21.99	0.55
4.19	-20.75	-5.99
8.21	-16.71	-11.73
11.12	-10.41	-15.88
12.52	-2.70	-17.88
12.24	5.37	-17.48
10.30	12.71	-14.71
6.97	18.34	-9.95
2.70	21.49	-3.86
-1.94	21.74	2.76
-6.31	19.05	9.01
-9.83	13.79	14.04
-12.02	6.67	17.17
-19.21	-5.90	27.43
-16.17	-19.01	23.09
-10.33	-22.83	14.76
-2.71	-33.67	3.88
5.38	-32.68	-7.68
12.54	-26.05	-17.90
17.53	-14.90	-25.03
19.49	-1.19	-27.83
18.08	12.74	-25.82
13.55	24.46	-19.35
6.67	31.95	-9.53
-1.36	33.92	1.94
-9.16	30.02	13.08
-15.37	20.93	21.95
-18.92	8.23	27.02

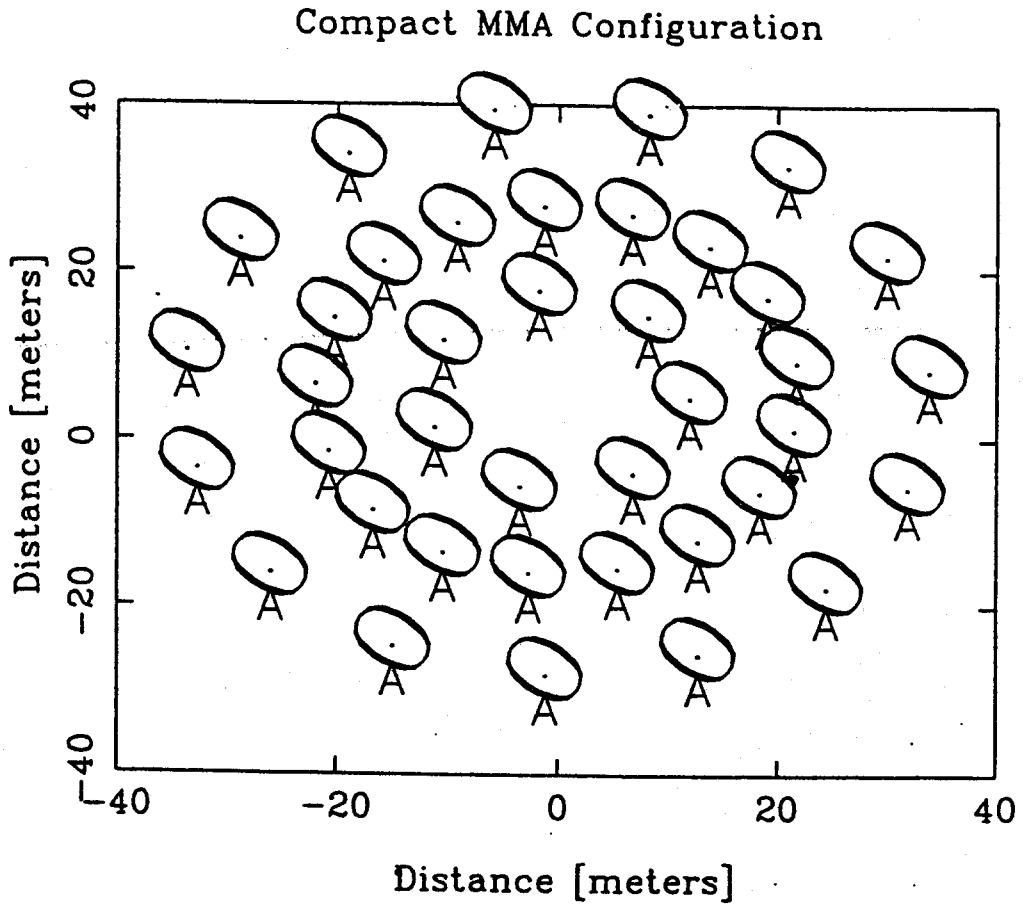
Compact MMA Configuration
Distance [meters]
40
20
0
-20
-40
-40
-20
0
20
40
Distance [meters]

Fig. 1

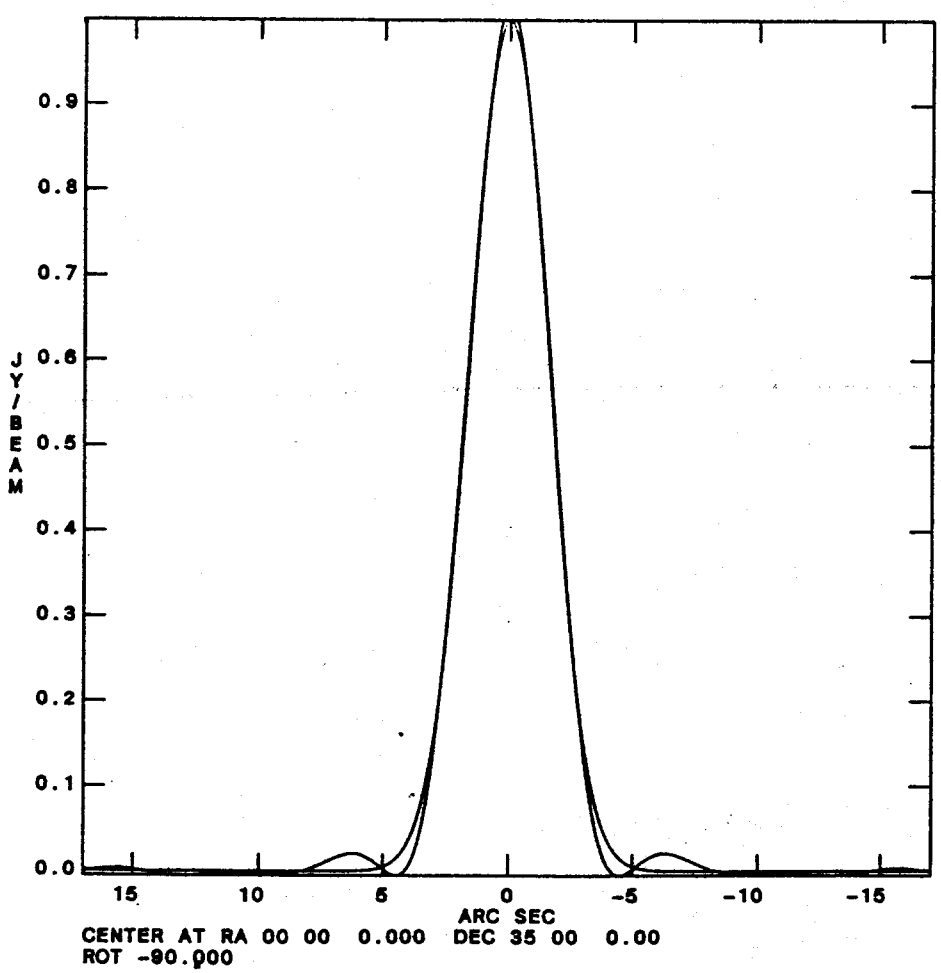
BEAM
0.9
0.8
0.7
0.6
0.5
0.4
0.3
0.2
0.1
0.0
15
10
5
0
-5
-10
-15
ARC SEC
CENTER AT RA 00 00 0.000 DEC 35 00 0.00
ROT -90.000

Fig. 2

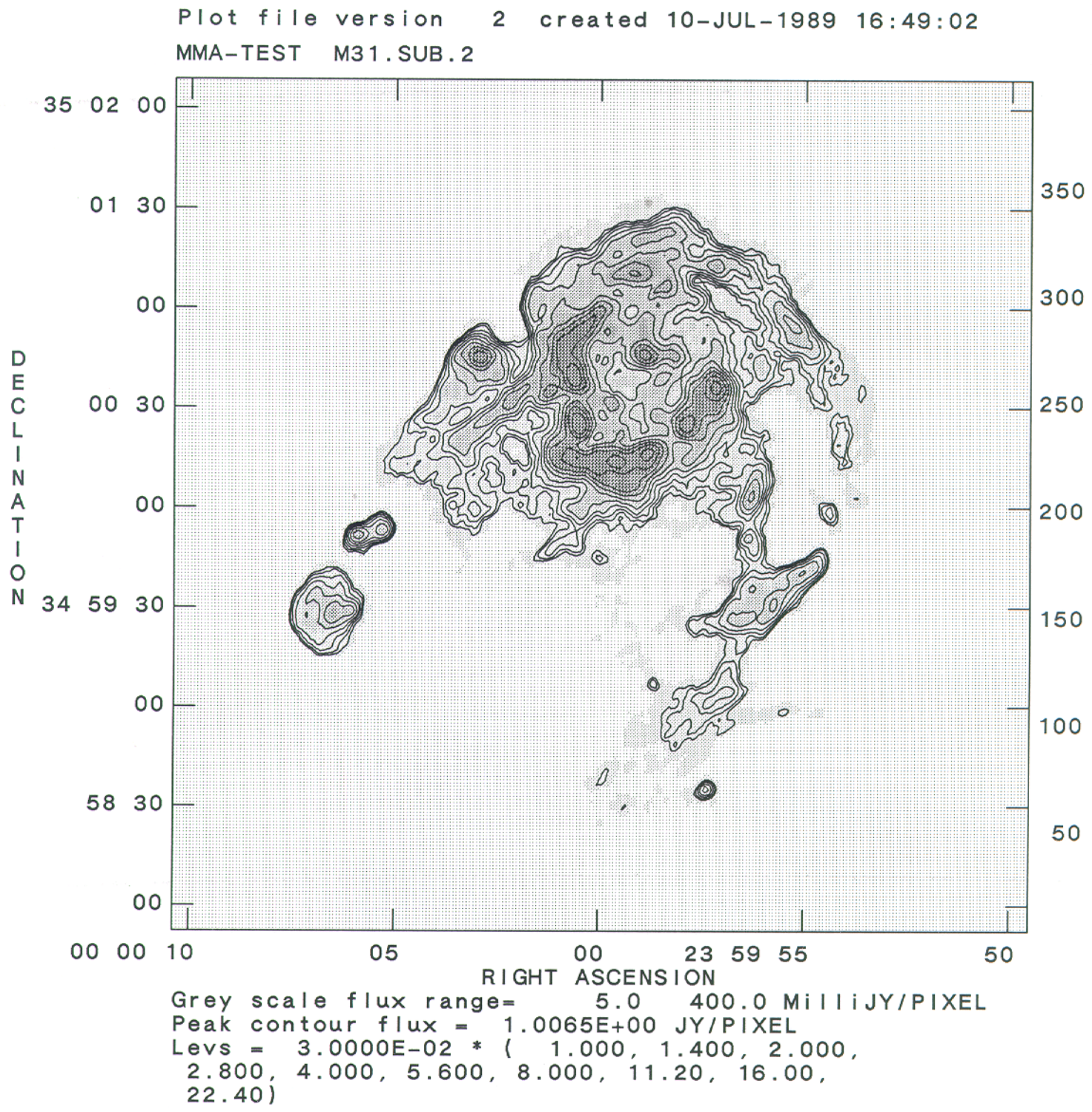
Plot file version 2 created 10-JUL-1989 16:49:02
MMA-TEST M31.SUB.2
35 02 00
01 30
00
00 30
00
34 59 30
00
58 30
00
DECLINATION
350
300
250
200
150
100
50
00 00 10
05
00
23 59 55
50
RIGHT ASCENSION
Grey scale flux range= 5.0 400.0 MilliJY/PIXEL
Peak contour flux = 1.0065E+00 JY/PIXEL
Levs = 3.0000E-02 * (1.000, 1.400, 2.000,
2.800, 4.000, 5.600, 8.000, 11.20, 16.00,
22.40)

Fig. 3.

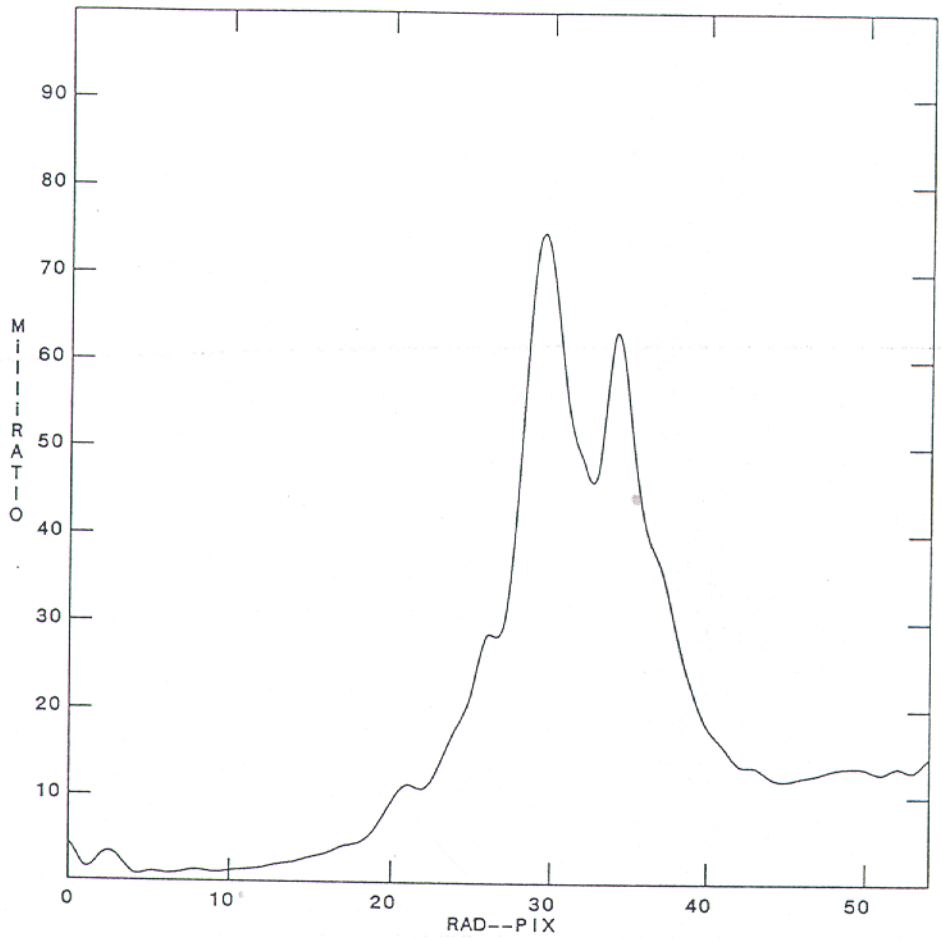
MILLIRATIO
90
80
70
60
50
40
30
20
10
0
10
20
30
40
50
RAD--PIX

Fig. 4

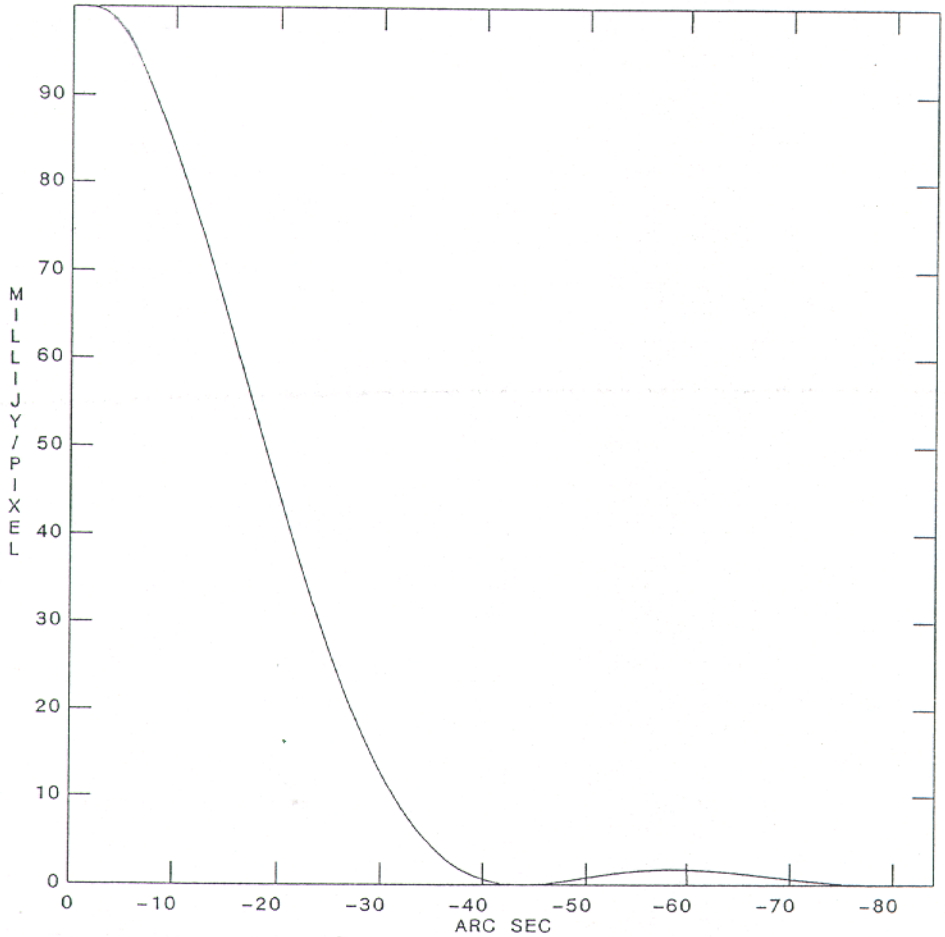
MILLIJY/PIXEL
90
80
70
60
50
40
30
20
10
0
0
-10
-20
-30
-40
-50
-60
-70
-80
ARC SEC

Fig. 5

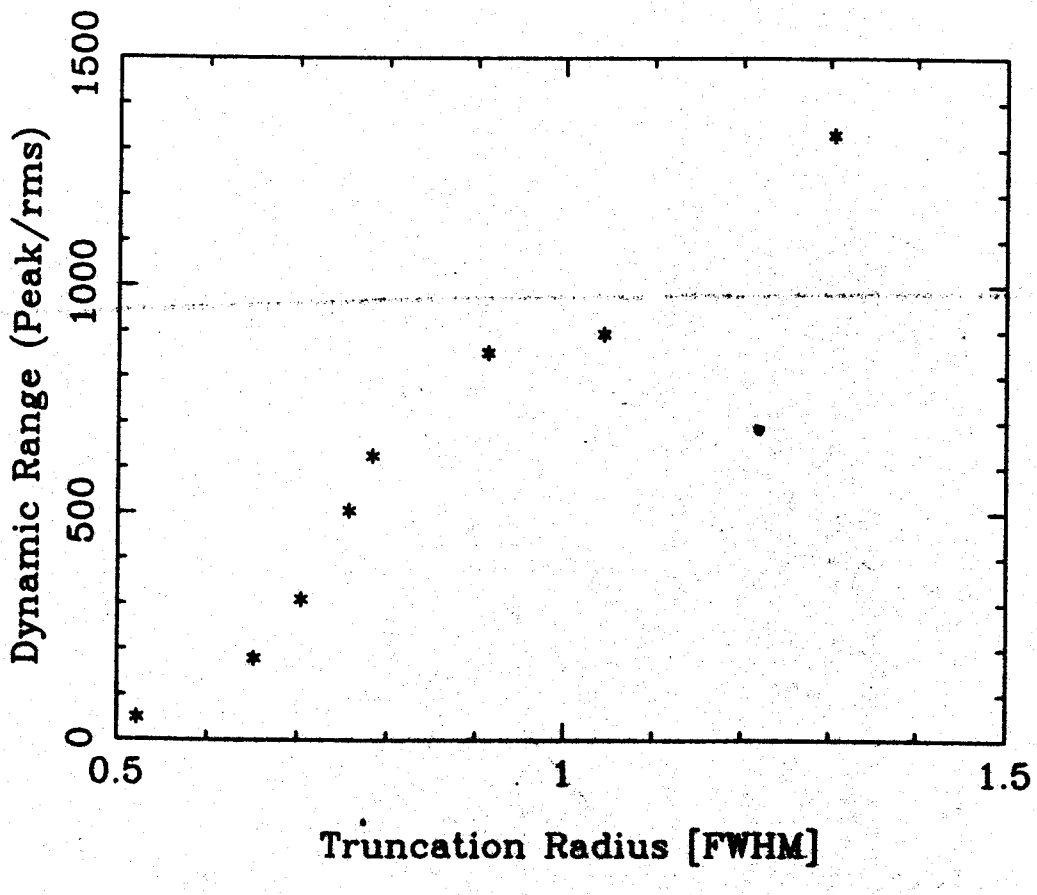
Dynamic Range of Fully Sampled Mosaic vs. Truncation Radius
Dynamic Range (Peak/rms)
0
500
1000
1500
0.5
1
1.5
Truncation Radius [FWHM]

Fig. 6a

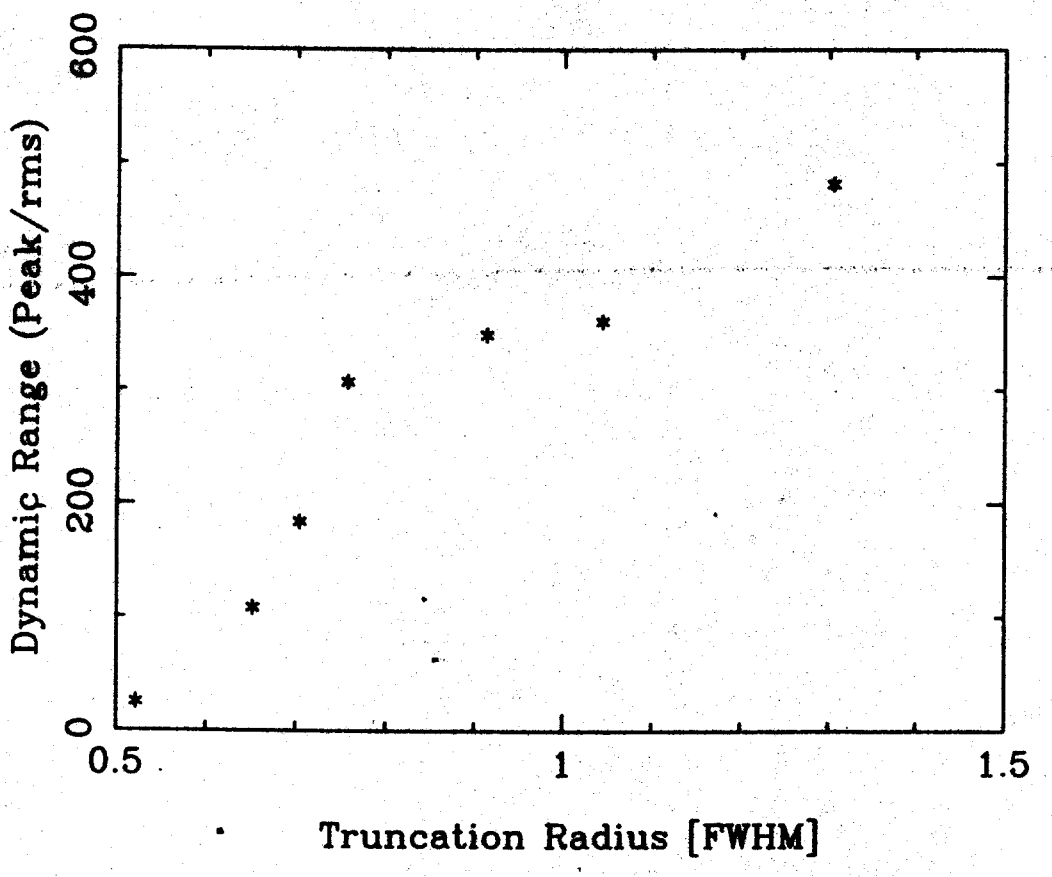
Dynamic Range of Partly Sampled Mosaic vs. Truncation Radius
Dynamic Range (Peak/rms)
0
200
400
600
0.5
1
1.5
Truncation Radius [FWHM]

Fig. 6b

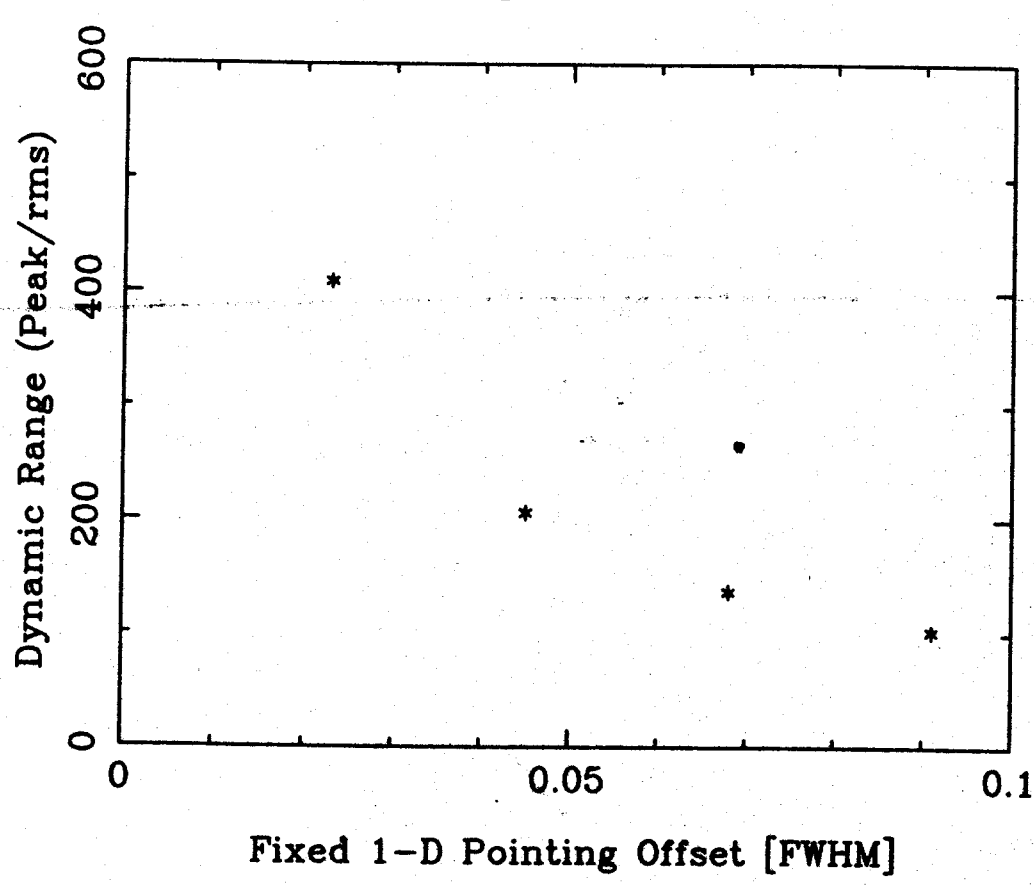
Dynamic Range of Fully Sampled Mosaic vs. Fixed Pointing Offset
Dynamic Range (Peak/rms)
600
400
200
0
0
0.05
0.1
Fixed 1-D Pointing Offset [FWHM]

Fig. 8a

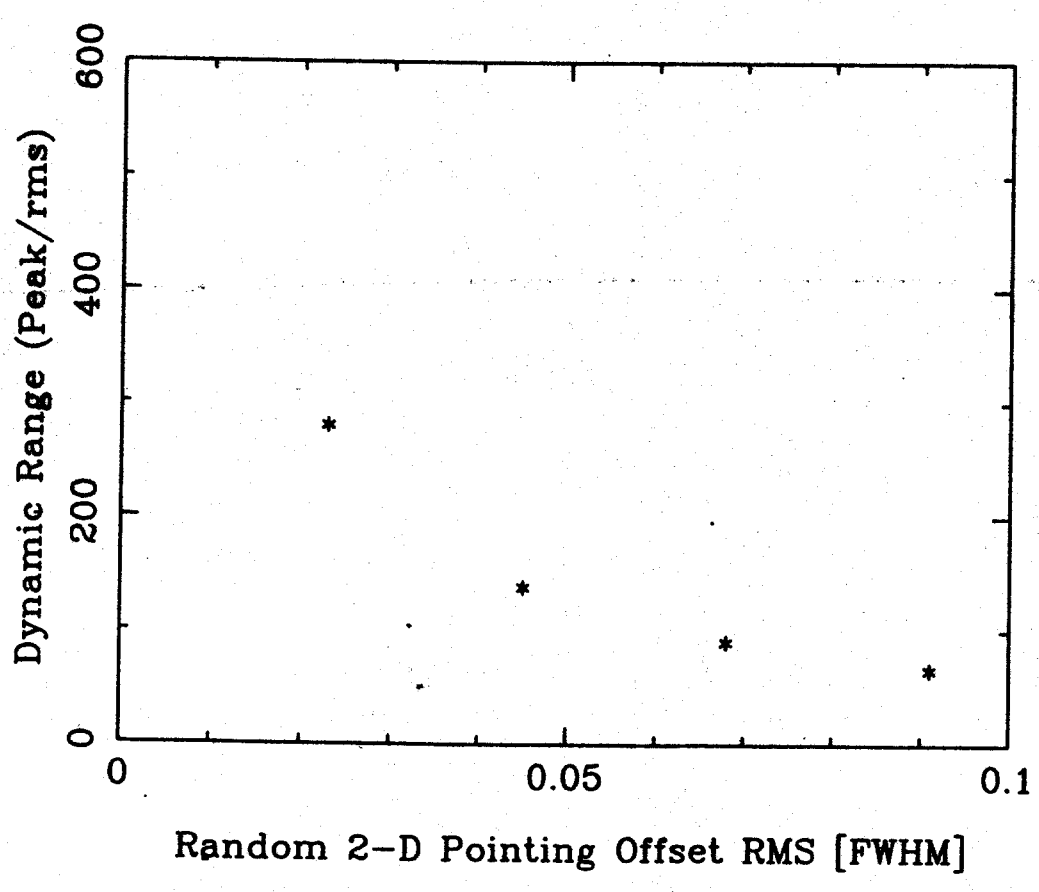
Dynamic Range of Fully Sampled Mosaic vs. Rand. Pointing Offset
Dynamic Range (Peak/rms)
600
400
200
0
0
0.05
0.1
Random 2-D Pointing Offset RMS [FWHM]

Fig 8b

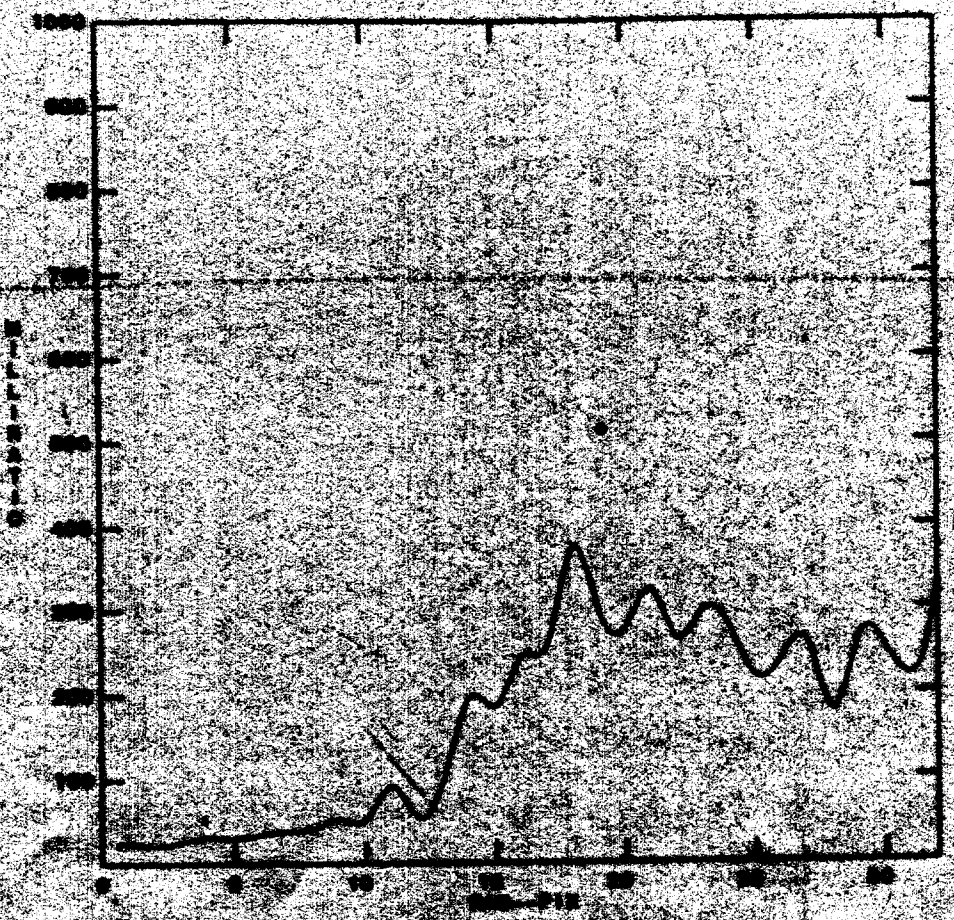

Fig. 7

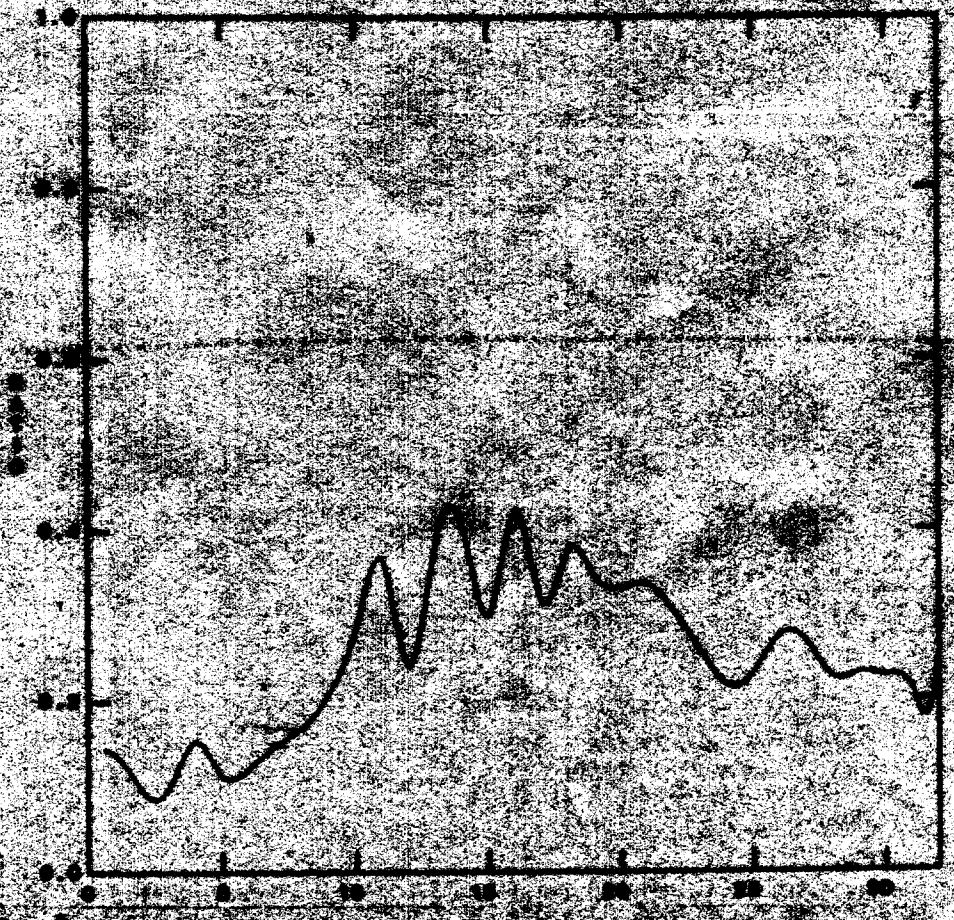

Fig. 9